This manuscript is currently under review for publication in
NATURE COMMUNICATIONS.

Please feel free to contact any of the authors; we welcome feedback

New flow relaxation mechanism explains scour fields at the end of submarine channels

F. Pohl,[1]* J. T. Eggenhuisen,[1] M. Tilston,[1] M. J. B. Cartigny,[2]

[1] Faculty of Geosciences, Utrecht University, P.O. box 80021, 3508 TA Utrecht, The Netherlands
[2] Department of Geography, Durham University, Lower Mountjoy South Road, DH1 3LE, Durham, UK
*Corresponding author: (florian.pohl63@gmail.com)

Abstract

In the ocean, particle-laden gravity flows, turbidity currents, flow in river-like channels across the ocean floor. These submarine channels funnel sediment, nutrients, pollutants and organic carbon into the ocean basins and can extend over 1,000's of kilometers. At the end of these channels, turbidity currents lose their confinement, decelerate and deposit their sediment load. This is what we read in textbooks. However, sea-floor observations have shown exactly the opposite: turbidity currents are prone to eroding the seafloor upon losing confinement. Such erosion features are commonly linked to a rapid flow transition associated with a hydraulic jump. This hypothesis has not been validated due to a lack of field measurements and scaling problems that prevented erosional turbidity currents to form in physical experiments. Here we use a state-of-the-art scaling method to produce the first experimental turbidity currents that erode upon leaving a channel. The experiments reveal a novel flow mechanism, here called 'flow relaxation' that explains the erosion. Flow relaxation is the rapid, internal flow deformation resulting from the loss of confinement, which enhances basal shearing of the turbidity current, thus promoting local scouring. This flow mechanism provides a new explanation of scour formation at the end of channels and its role in the propagation of submarine channel systems.

Introduction

Turbidity currents are particle-laden gravity flows that move downslope because of the density difference between the sediment-laden flow and the ambient water. They represent a major transport agent for sediment in the ocean, and turbidite deposits serve as a sink for organic carbon burial [1,2], as major reservoirs for hydrocarbons [3], and also as a depot for plastic debris [4,5]. On the ocean floor, turbidity currents typically transport sediment within confinements such as channels, which focus the flow and prevent deposition of the suspended sediment [6]. Upon leaving the channels, turbidity currents lose their lateral confinement and deposit their sediment load in lobate sediment bodies, forming the largest sediment accumulations on Earth [7]. While the sediment transport in channels and the deposition on lobes is reasonably well understood, it is not clear why these two systems are connected by a transition zone characterized by enhanced erosion, referred to as the channel-lobe transition zone (CLTZ) (Fig. 1a) [8].

It is surprising that the area downstream of a channel is marked by erosion. The lateral expansion and associated deceleration of turbidity currents upon leaving the channel would suggest deposition. Previous research has established that a turbidity current leaving a channel confinement spreads laterally, and that lateral spreading increases the overall friction of the flow, resulting in deceleration and deposition of suspended sediment [9,10]. Yet bathymetric surveys on modern CLTZs show repetitive erosive structures, so-called scour fields, instead of the anticipated deposits (Fig. 1a) [11–15]. These scour fields can be >100 km long with individual scours up to 20 m deep and 2,500 m long (Fig. 1c) [12,14]. Erosion of the ocean floor at the CLTZ inherently plays a critical role in the development and the propagation of channel systems (Figs. 1d and e) [16–20]. Although erosive features of CLTZs are well documented, the dominant conceptual model to explain their genesis remains speculative and has not been subjected to rigorous experimental evaluation.

The favored hypothesis explaining erosion at the channel terminations is the occurrence of a hydraulic jump (i.e. the transition from Froude supercritical to Froude subcritical flow) as the turbidity current leaves the lateral confinement [8,14,21]. A hydraulic jump is expected to increase in the erosion potential of the flow, as turbulence in the flow is increased locally [21–23]. Russell and Arnott [24] explain scouring in the CLTZ by the impingement of vortices that were produced by the hydraulic jump. However, there is no study that confirms the link between erosion processes and such hydraulic jump.

Here we use the newly developed Shields scaling approach [25] to directly observe the erosion mechanism in a turbidity current leaving a lateral confinement in an experiment set-up (Fig. 2a). Additionally, we conduct a reference experiment in which the flow remained confined over the entire slope (Fig. 2b). The experiment method allows to observe the dynamic interaction between the turbidity current and the sea-floor in relation to the loss of confinement. The observed incision at the CLTZ is explained by a flow mechanism which we term ‘flow relaxation’. Flow relaxation results from the loss of lateral support of the turbidity current by the channel walls leading to a crucial mechanism for channel propagation on the ocean floor.

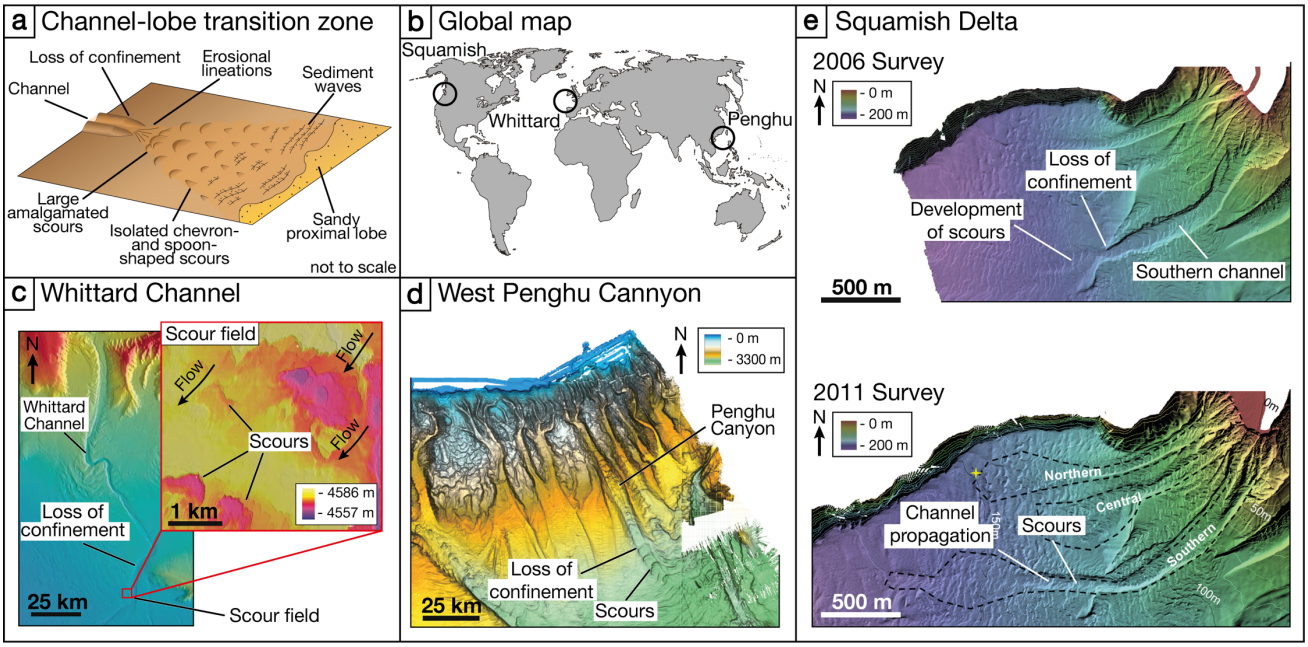

Fig. 1. Examples of systems with a loss of confinement. a-e, (**a**) Sketch of a channel-lobe transition zone based on bathymetrical surveys. Modified from [14]. (**b**) Global map showing the locations of the systems shown in panel c-e. (**c**) Bathymetry map of the Whittard Channel. The ocean floor downstream of the channel termination is characterized by scour fields [12]. (**d**) The West Penghu canyon in the South China Sea. Downstream of the loss of confinement the ocean floor is marked by a line of scours indicating erosion and the progradation of the canyon [40]. (**e**) The Squamish Delta. In the upper bathymetry map, the channel termination is marked by a rapid loss of confinement [39]. The lower bathymetry map was obtained 5 years later and shows how erosion has led the propagation of the channel by ~400 m [37].

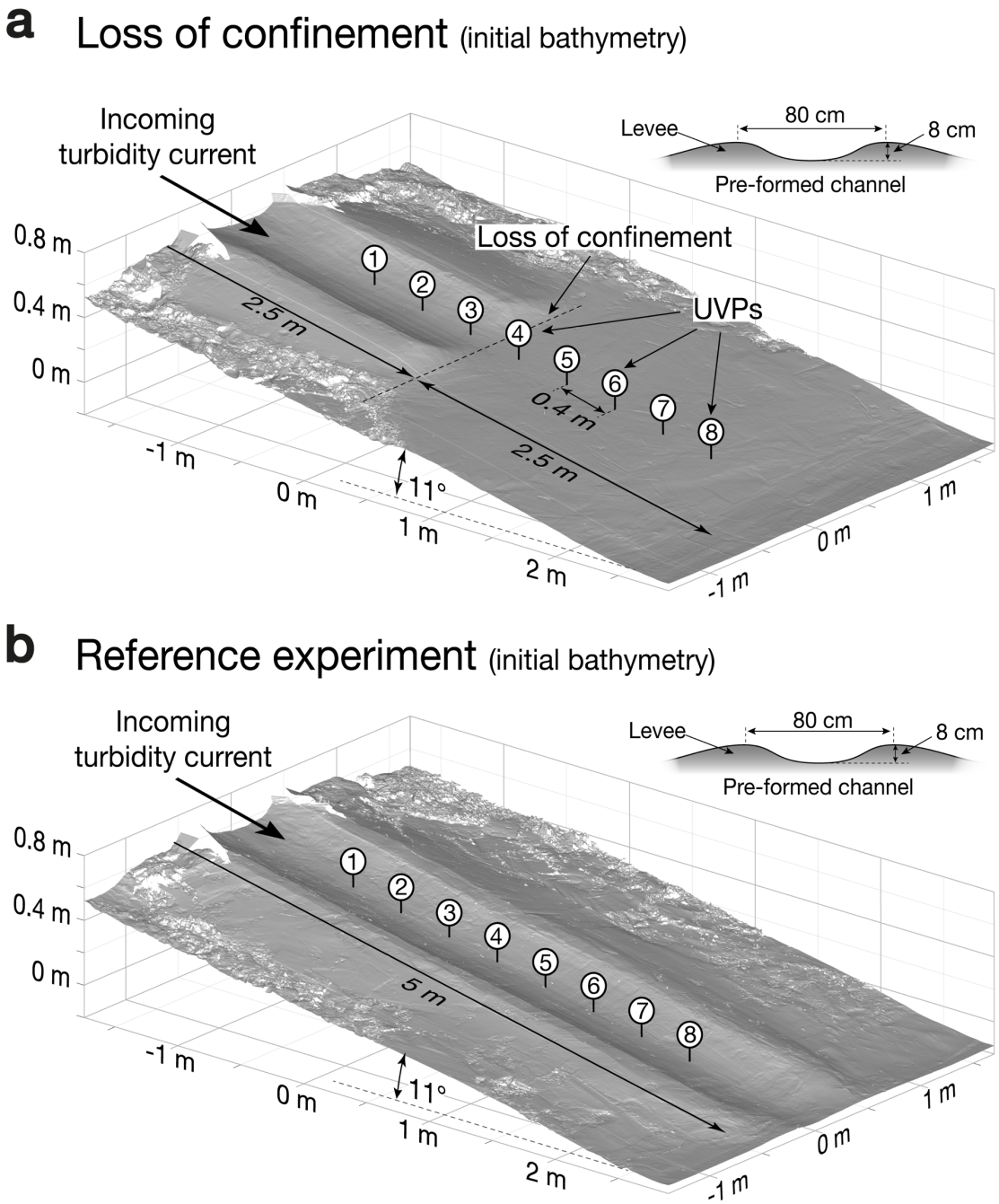

Fig. 2. Digital-elevation-models of the initial bathymetry. a,**b**, (**a**) The experiment with loss of confinement. The loss of confinement was generated by a decrease of the levee height 2.5 m downstream of the inlet box. (**b**) The reference experiment with a continuous pre-formed channel over the entire length of the slope. The substrate in both experiments was equivalent to that of the sediment mixture used to generate the experiment currents. The channel dimensions, as well as the input conditions of the incoming turbidity current, were identical in both experiments. UVP: Ultrasonic Velocimetry Probe.

Results

The experiment results show the anticipated enhanced erosion downstream of the loss of confinement (Fig. 3a). Upstream of the loss of confinement both experiments display the expected similar behavior (Figs. 3a, b, and c). Upon losing confinement, however, the unconfined flow incised deeper along the down-flow trajectory than in the reference experiment without the loss of confinement. The incision in the center was flanked by deposition of a ~2 cm high ridge on each side (Fig. 3a). In contrast, the reference experiment showed less incision and no depositional ridges (Fig. 3b). The overall morphologic development of incision flanked by depositional ridges generated a new confinement.

The development of the self-confinement propagated downstream over time suggesting an association of enhanced erosion with incipient channel development. The propagation of the confinement was captured by the velocity probes (Fig. 3d). The enhanced erosion rate (i.e. change in bed elevation) decreased to zero at UVP 4 downstream of the loss of confinement over the first ~40 s of the experiment (Fig. 3d), when the self-confinement was established. Further downstream, at UVP 5, the initial erosion rate decreased to zero over a longer time period of ~80 s (Fig. 3d), implying a delayed establishment of the self-confinement at this location. Hence, the establishment and the propagation of the self-confinement in the experiment was driven by on-axis erosion and off-axis deposition downstream of the loss of confinement.

The turbidity current immediately spread and thinned upon leaving the confinement, resulting in an increased basal shearing and erosion potential of the flow. The velocity of the turbidity current was captured by 8 velocity probes aligned along the channel thalweg (Figs. 2a and b). Each of the probes collected a full vertical velocity profile of the flow (Figs. 4a and b). The turbidity current accelerated down the channel as it entered the setup. Downstream of the loss of confinement the flow decelerated (Fig. 4c). Deceleration was accompanied with a decrease in flow thickness due to lateral spreading upon leaving the channel (Fig. 4d). However, due to the thinning of the flow, the velocity gradient at the flow base is increased (cf. Fig. 4a), which enhances the friction between the flow and the bed, i.e. the bed shear velocity (Fig. 4e). The increased shear velocity upon thinning of the flow is responsible for the enhanced erosion downstream of the loss of confinement.

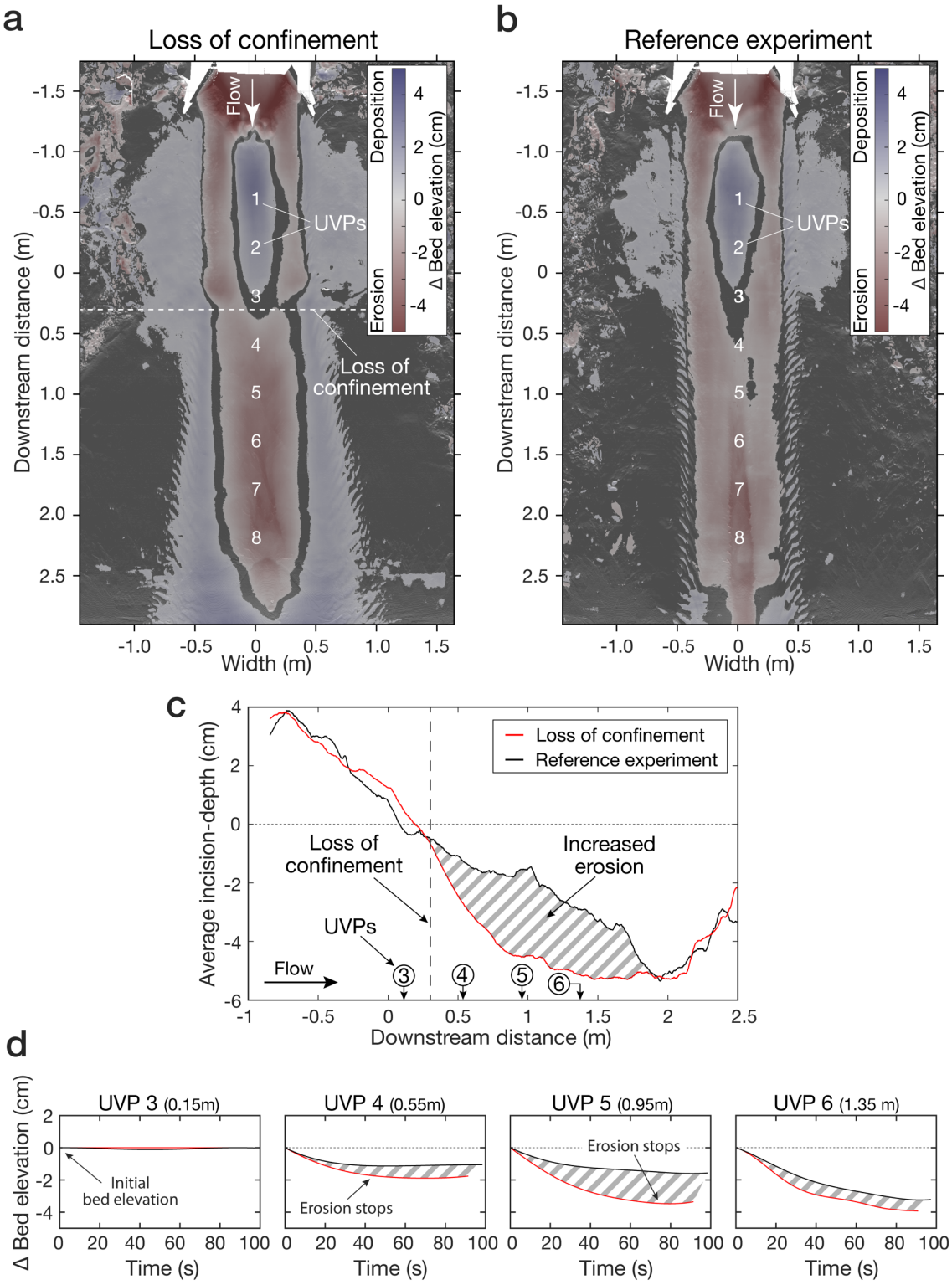

Fig. 3. Erosion and deposition in the two experiments. a-d, (**a**), Map showing erosion and deposition in the experiment with the loss of confinement. (**b**) Erosion and deposition in the reference experiment. (**c**), Laterally averaged incision-depth of a 30 cm wide strip along the channel thalweg. Erosion in the experiment increased with the loss of confinement. (**d**), Bed-elevation change during the experiments captured by the UVPs. Bed-elevation change was generally higher in the experiment with the loss of confinement than in the reference experiment. The difference was highest below UVP 5, which was located 0.95 m downstream of the loss of confinement.

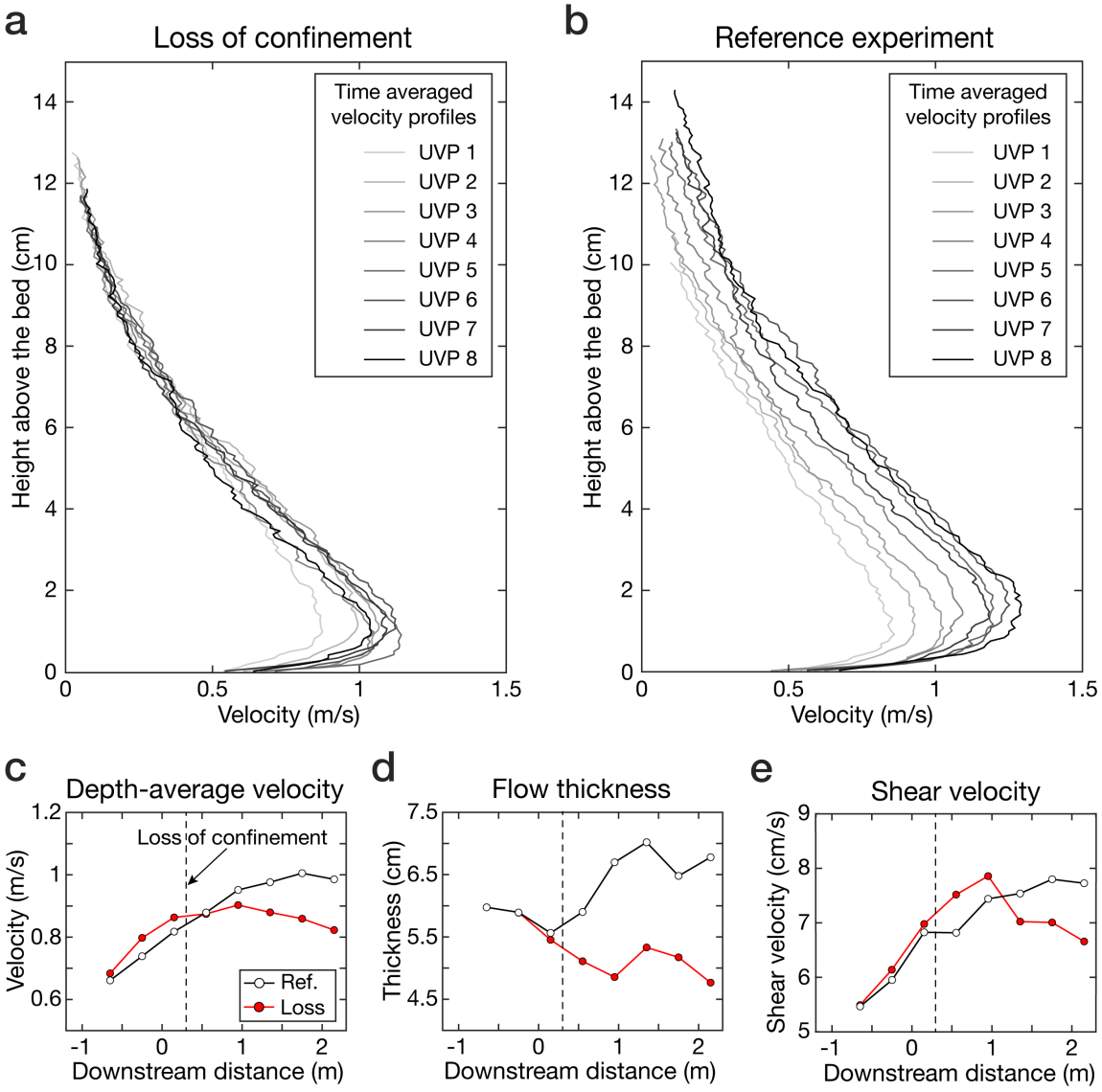

Fig. 4. Flow-dynamic parameters captured by the velocity probes. a-e, (**a**), Time-averaged velocity profiles for the turbidity current in the experiment with loss of confinement. (**b**) Time-averaged velocity profiles for the turbidity current in the reference experiment (see figure 2 and 3 for probe locations). (**c**), Depth-averaged velocity downstream of the loss of confinement the turbidity current decelerated and was slower than the current in the reference experiment. (**d**), Flow thickness. After leaving the confinement the turbidity current immediately thinned. (**e**), Shear velocity. Shear velocity was slightly increased downstream of the loss of confinement and decreased farther downstream.

Discussion and conclusions

As previously noted, the morphological changes at the loss of confinement result in rapid flow deformation, which in turn triggers enhanced erosion. Our results indicate that this deformation manifests itself through the vertical thinning and lateral spreading of the flow field. The mechanism leading to this transformation is explained through the concept of flow relaxation, which describes the reaction of the flow to the development of strong lateral pressure gradients upon exiting the channel (Figs. 5a and b).

We propose that changes in the lateral pressure gradient at the base of the flow explain the concept of flow relaxation. Within turbidity currents, hydrostatic pressure is increased by the mass of the overlying suspended particles, and since particle concentration decreases from the bed to the top of the current, so does the pressure [26]. The lateral pressure gradient is zero in a channelized flow, due to the absence of horizontal density gradients (Fig. 5a) [27]. When the flow loses confinement, a lateral pressure gradient develops between the dense current and the ambient fluid that drives flow spreading (Fig. 5b). The lateral pressure gradients are strongest at the bottom of the current, which explains the rapid basal evacuation and the lowering of the high velocity core. It is the lowering of this high velocity core that leads to an increase of the near-bed velocity gradient and bed shear velocity (Figs. 4a, d, and e), resulting in scour development. In this model the area between the proximal and distal regions of the scour field is interpreted as the distance over which the current re-equilibrates to the new unconfined flow conditions. In summary, rapid flow deformation and associated scour formation that occurs over this re-adjustment range is explained through changes in lateral pressure gradients as explained in the flow relaxation model (Figs. 5a and b).

Research to date has tended to ascribe the formation of scour fields in CLTZs to hydraulic jumps [8,14,15,21,28,29]. In this model scours would form because of enhanced turbulence created by a hydraulic jump [21–23]. In our experiments, we did not observe a hydraulic jump as the flow is thinning upon leaving the confinement (Fig. 4d), while a hydraulic jump would result in thickening of the flow [29]. Previous experiments in saline density flows without suspended particle have observed a hydraulic jump at the channel termination [20]. However, this hydraulic jump was correlated with late-stage topographic forcing through channel mouth bar development rather than the loss of confinement. Moreover, a single hydraulic jump would form a single scour rather than scour fields as observed in CLTZs (Figs. 1a and c). Monitoring of saline flows in the Black Sea channel have revealed that each scour is associated with an individual hydraulic jump [15,30]. Consequently, Dorrell et al. [15] have evoked the presence of a 'hydraulic-jump-array' associated with the formation of a scour field in CLTZs. However, the density structure of the Black Sea saline flows is different from the density structure of a turbidity current [31–33], and therefore it remains questionable whether such hydraulic-jump-array model translates across to turbidity currents. Furthermore, the hydraulic jumps in the Black Sea formed within the confinement of a channel, rather than at the loss of confinement of the CLTZ [15,30]. Finally, a third model explains multiple scours by the impingement of vortices into the ocean floor beneath a hydraulic jump [24]. In this model, each individual impingement would form a scour. However, scour formation by impingement of vortices was never produced in

experiments. Overall, the association of scour fields in CLTZs with hydraulic jumps remains open for debate.

Flow relaxation is a mechanism that well explains the formation of scour fields in CLTZs. Instead of going through a hydraulic jump, the flow relaxes upon leaving the confinement, enhancing the basal shearing of the turbidity current (Figs. 4a and e). This increases the erosion of the sediment bed by the flow, and triggers scour formation [34]. Hence, the likelihood of the formation of scours is increased over the entire area in which the flow relaxes. In this area, the locations of individual scours are likely determined by irregularities and inhomogeneities on the ocean floor [34], thereby explaining the observed scour fields in CLTZs.

Submarine channels can grow to extraordinary lengths, like the Northwest Atlantic Channel which extends over up to ~3,800 km [35]. Additionally, these submarine channels can propagate at exceptional rates of up to ~500 m/yr in the Amazon system [36] or ~80 m/yr. in the much smaller Squamish system [37]. This rate suggests a very effective channel propagation mechanism. The nature of this propagation mechanism is much debated, where attention has so far focused on whether the propagation of submarine channels is dominatly due to erosion or deposition [16–19,25,38]. Hamilton's et al. [20] experimental saline density flows show an increase in the flow sediment transport capacity at channel mouth, and they proposed erosion as the impetus for sustained channel propagation. Our results provide the physical processes that drive the erosion and demonstrate the applicability of the processes in sediment-laden flows, such as turbidity currents. As the flow relaxes at the channel termination, it incises in the center and deposits levee-shaped sediment bodies off-axis to both sides, efficiently forming a self-confinement (Figs. 3a and 5b). The self-confinement provides lateral support to the flow, which results in a decrease of the lateral pressure gradient, and maintains the flow thickness. Hence, the self-confinement is damping the effect of the flow relaxation and thus the erosion potential of the flow. Self-confinement establishes until an equilibrium channel shape is reached, thereby extending the channel further across the ocean floor.

Our model provides a mechanism explaining the propagation of a channel in the Squamish ProDelta. A bathymetry map of the Squamish Delta that was monitored in 2006, showed that the Southern Channel terminated with a rapid loss of confinement (Fig. 1e) [39]. A subsequent bathymetry study in 2011 revealed propagation of the Southern Channel over a distance of ~400 m (Fig. 1e) [37]. Channel propagation was generated by incision into the underlying substrate downstream of the rapid loss of confinement and, hence, driven by erosion comparable to the channel propagation in our experiments (Fig. 3a).

Our results provide measurements of a turbidity current that enhances its erosion potential by leaving a channel. Upon leaving the channel confinement the turbidity current laterally spreads and thins, which causes an increase in the bed shear stress and erosion. The here introduced model of flow relaxation provides a flow dynamic process that is pivotal for the development of scour fields in CLTZs, and plays a central role in the propagation of submarine channels.

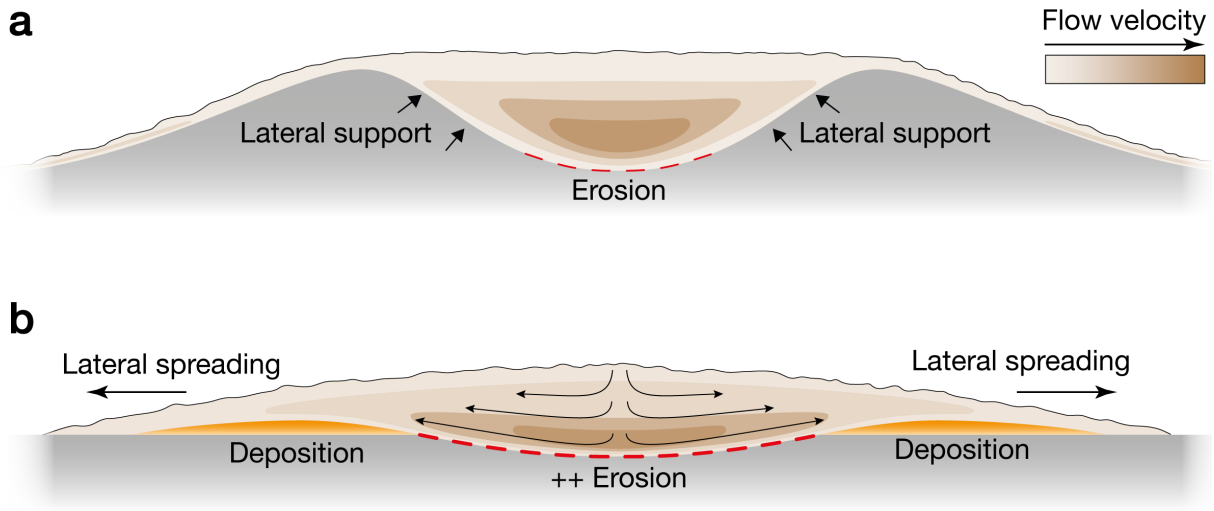

212
213 **Fig. 5. Illustration of the flow relaxation model. a**,**b**, (**a**) Flow confined in a channel. The
214 channel side-walls counteract the near-bank lateral pressure differences within the flow,
215 resulting in a lateral pressure gradient of zero. Note lateral and vertical variations in the flow
216 velocity field, after [27]. (**b**) A flow that 'relaxes' upon leaving a confinement. The loss of lateral
217 support by the channel flanks results in a lateral pressure gradient within the flow, and hence,
218 lateral spreading and thinning. This shifts the height of the maximum velocity bed-wards,
219 increases the shear stress at the bed, resulting in erosion. Lateral to the incision, levee-shaped
220 sediment bodies are deposited due to the lateral decrease in flow velocity.

221 ## Materials and Methods

222 ### Scaling approach

223 The turbidity currents were downscaled from natural to experiment size by using Shields
224 scaling [25]. This technique relies on two scaling parameters: (1) The Shields parameter, which
225 is kept close to natural values, and (2), the boundary Reynolds number, which is relaxed as long
226 as rough to transitionally rough boundary layer conditions are maintained (Fig. S1). Together,
227 these two parameters predict whether the current will erode or deposit sediments and whether
228 the particles will be transported as bedload or suspended load.

229 The Shields parameter describes the ratio between the shear stress and the gravity force acting
230 on particles [41]:

231 $$\theta = \frac{\rho_t u_*^2}{\left(\rho_s - \rho_w\right) g d_t} \,, \tag{1}$$

232 where ρ_s is the density of the suspended sediment (quartz sand with 2650 kg/m³), ρ_w the density
233 of water (1000 kg/m³), d_t the grain size of the suspended sediment, g the gravitational force
234 (9.81 m/s²), and u_* the shear velocity (Eq. 3). The density of the turbidity current ρ_t is:

235 $$\rho_t = \left(\rho_s - \rho_w\right) C + \rho_w \,, \tag{2}$$

236 with C as the sediment concentration. The shear velocity u_* can be derived from the shape of
237 the velocity profile below the velocity maximum U_{max}, by assuming a logarithmic velocity
238 profile between the bed and the height of the velocity maximum h_m [25,42–44]:

239 $$u_* = U_{\max} \kappa \left(\ln\left(\frac{h_m}{0.1 d_{90}} \right) \right)^{-1} \,, \tag{3}$$

240 where κ is the von Kármán constant with a value of ~0.4. The d_{90} is derived from the grain-size
241 distribution in the turbidity current.

242 Studies of natural turbidity currents revealed a typical value for the Shields parameter of 1 – 10
243 (Fig. S1) [2,45]. In our experiments, we meet these values by varying the sediment concentration
244 and the velocity of the flow by varying the slope accordingly.

245 The boundary Reynolds number Re_p controls the hydraulic conditions of the viscous sub-layer,
246 from hydraulically smooth ($Re_p < 5$), to transitional ($5 < Re_p < 70$), to hydraulically rough (Re_p
247 > 70) [46]. In the hydraulically rough regime, the viscous sub-layer is dominated by turbulent
248 forces, whereas in a hydraulically smooth regime the viscous sub-layer is dominated by viscous
249 forces. Studies report a transitionally rough regime for natural turbidity currents (Fig. S1) [2,47].
250 The value of the Re_p is given by the ratio of the grain size to the thickness of the viscous sub-
251 layer:

252 $$\mathrm{Re}_p = \frac{u_* d_b}{\nu} \quad , \qquad (4)$$

253 where d_b is the grain size of the sediment of the bed, and ν is the kinematic viscosity of clear
254 water at 20°C (1 x 10^{-6} m²/s). In the experiments, we meet the transitionally rough hydraulic
255 regime by using a fine grain size (d_{10} = 35 µm, d_{50} = 133 µm, d_{90} = 214 µm) for the sediment
256 of the bed (Fig. S2). We also use the same grain size for the suspended sediment of the turbidity
257 current to avoid changes in bed grain size due to deposition from the flow.

258

259 **Experiment setup and procedure**
260 The turbidity currents were released into a 11 m x 1.3 m x 6 m (length x height x width) basin,
261 filled with fresh water (Fig. S3). The floor consists of a 5 m long slope of 11°, followed by a
262 horizontal basin floor of 6 x 6 m at the base of slope (Fig. S3). The turbidity current was
263 generated from a 0.9 m³ mixture of sediment and water prepared in a separate mixing tank using
264 quartz sand with a mean density of 2650 kg/m³, particle diameter (d_{50}) 133 µm (Fig. S2), and
265 volumetric concentration of 17 %. The mixture was pumped into the basin with a radial-flow
266 pump with a constant discharge of 30 m³/h. The discharge was monitored with an
267 electromagnetic flow-meter (Krohne Optiflux 2300) (Fig. S4). The turbidity current entered the
268 setup at the upper end of the slope through an inlet box and flowed downslope driven by its
269 excess density.

270 The initial bathymetry in the experiment consisted of an 11° sloping basin floor with a pre-
271 formed channel that abruptly loses lateral confinement (Fig. 2a). The channel was formed by
272 building confining levees on the slope, and the channel dimensions were 80 x 8 cm (width x
273 depth). Both the levees and the slope were made of loose sand that had the same grain-size
274 distribution as the sand used for the turbidity current (Fig. S2). During the experiment, the bulk
275 portion of the flow was contained by the channel, with minimal overspill across the levee crests.

276 In a reference experiment, a pre-formed channel with identical dimensions was used, while the
277 channel extended over the entire length of the sloping basin floor (Fig. 2b). Besides the
278 difference in channel length, all other parameters were kept identical in the two experiments.

279

280 **Digital elevation model**
281 After the release of an experiment current, the basin was drained to expose the deposits. The
282 deposits were scanned by a laser scanner with a measurement accuracy of <0.5 mm. From the
283 laser scan a Digital Elevation Model (DEM) with a horizontal grid spacing of 2 x 2 mm was
284 created. Subtraction of the post-flow DEM from the pre-flow DEM yields a map of the
285 experiment current's deposition and erosion patterns (Figs. 3a and b).

286 To quantify the erosion during the two runs the average incision-depth was calculated (Fig. 3c).
287 Incision-depth was averaged along the width of a 0.3 m wide corridor, which was aligned within
288 the channel thalweg along the downstream direction. Incision values were laterally averaged to

remove “noise" associated with local variations in incision depth and therefore represent bulk-averaged trends.

UVP data acquisition and processing

An array of 8 Ultrasonic Velocimetry Profilers (UVPs) was installed along the channel axis to capture changes in the flow field associated with the abrupt loss of confinement (Figs. 2a and b); UVP acquisition settings are given in Table S1. The downstream spacing between individual UVPs was 0.4 m and the probes were set 0.15 m above the bed, facing the upstream direction at an angle of 60° with respect to the basin’s initial bed configuration (Fig. S5a). Each UVP measures the velocity of sediment grains along the probe’s axis, and the bed-parallel velocity component is obtained by trigonometric calculations (Fig. S5a); this calculation assumes that the bed-normal component of velocity is zero. The bed-parallel velocity against time for all UVPs is shown in figure S6 for experiment with the loss of confinement, and in figure S7 for the reference experiment. The interface between the flow and sediment bed was discernable as a sharp decrease in velocity (Figs. S6 and S7). The vertical bed position was tracked over time, yielding erosion and deposition rates below individual UVPs (Fig. 3d).

Time-averaged profiles were generated for the body of the current, where the flow is generally steady (Fig. 4a and b). The velocity measurement of the current head and of the tail were omitted for the time-averaging (Figs. S6 and S7). The time-averaged profiles were then smoothed using a Fournier fitting function to remove spurious spatial velocity fluctuations linked with the UVP’s sampling resolution to determine the magnitude U_{max} and the height h_m of the velocity maxima. The flow thickness h is defined here as the height at which the velocity u is half the velocity maximum U_{max} (Fig. S5) [48–51]. The depth-averaged velocity was averaged between the bed and the flow thickness h.

Supplementary materials

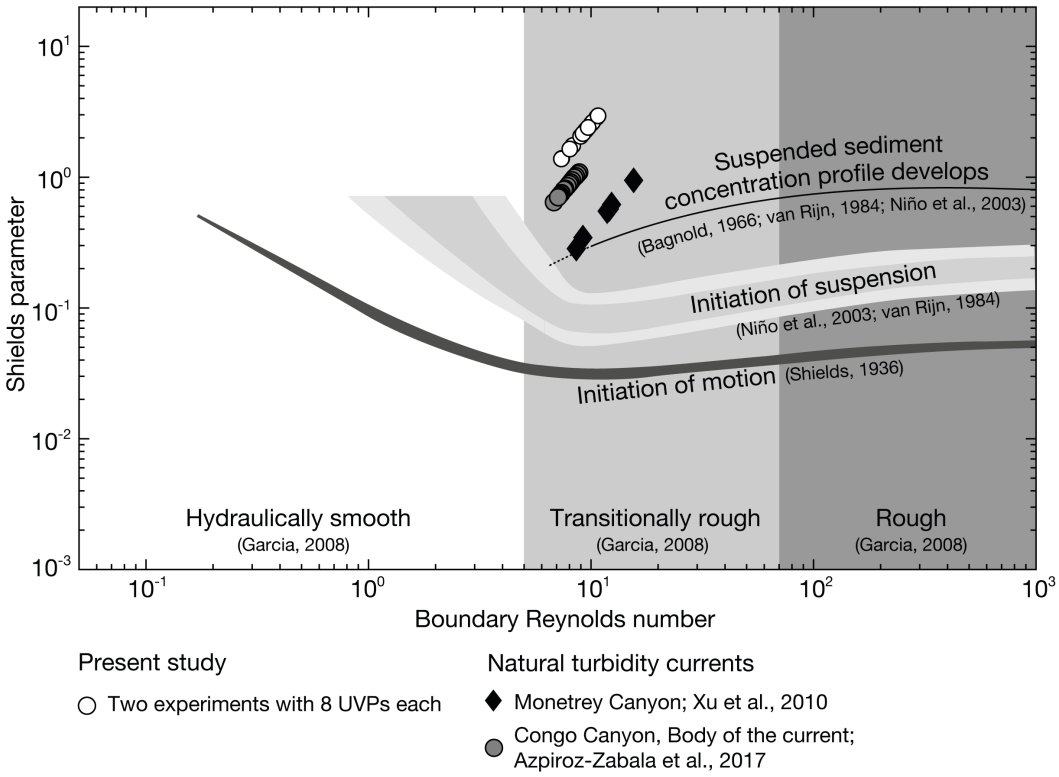

Fig. S1. Shields mobility diagram. Describes the dominant sediment transport mode for a given set of hydrodynamic conditions. Modified after [41] and [25]. Natural flows were monitored in the Monterey Canyon [45], and the Congo Canyon [2]. For calculation of the point for the Congo Canyon, the body of the current was used. Regime boundaries after: [41,43,46,52,53]

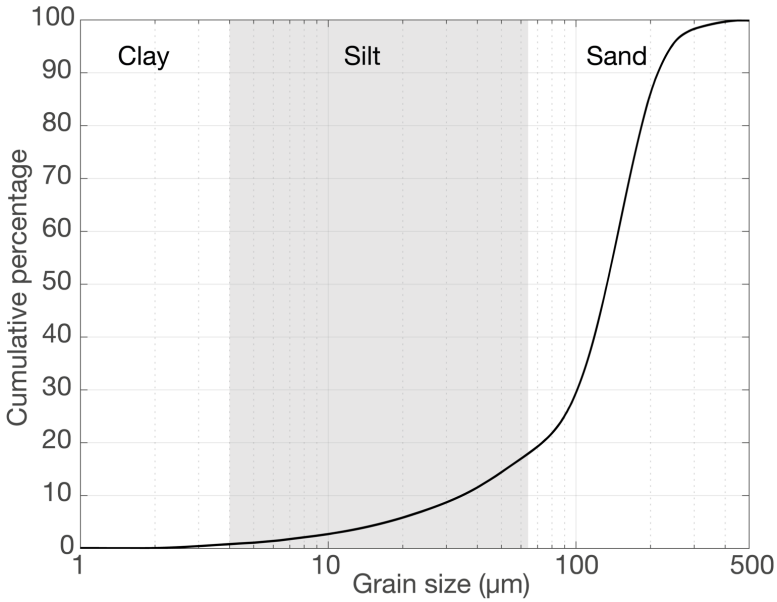

Fig. S2. Cumulative grain-size distribution. Sand of identical grain size was used for the floor of the flume tank and for the suspended sediment of the turbidity current. Grain size was measured with a laser particle sizer (Malvern Mastersizer 2000).

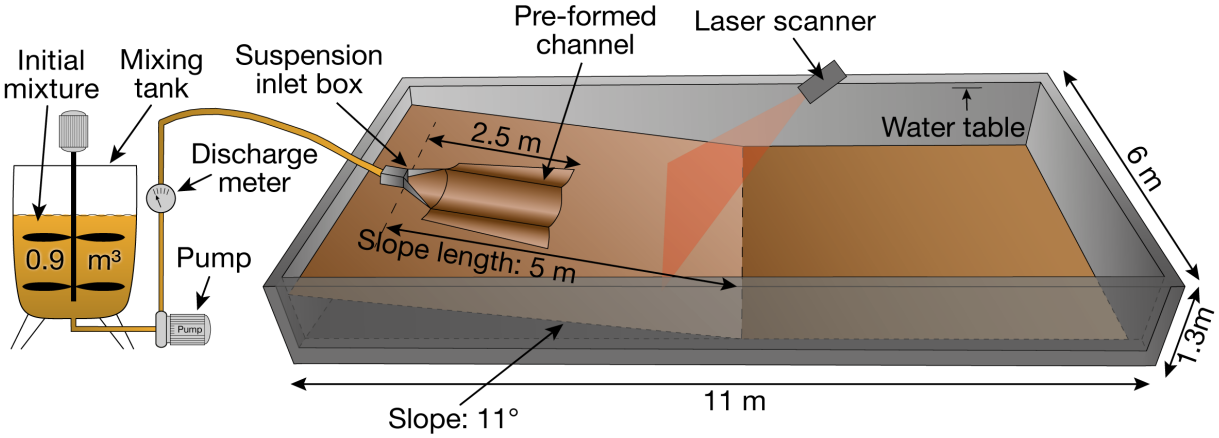

Fig. S3 Schematic drawing of the experiment setup. Note that the length of the reference (no loss of confinement) experiment extended 5 m further downslope.

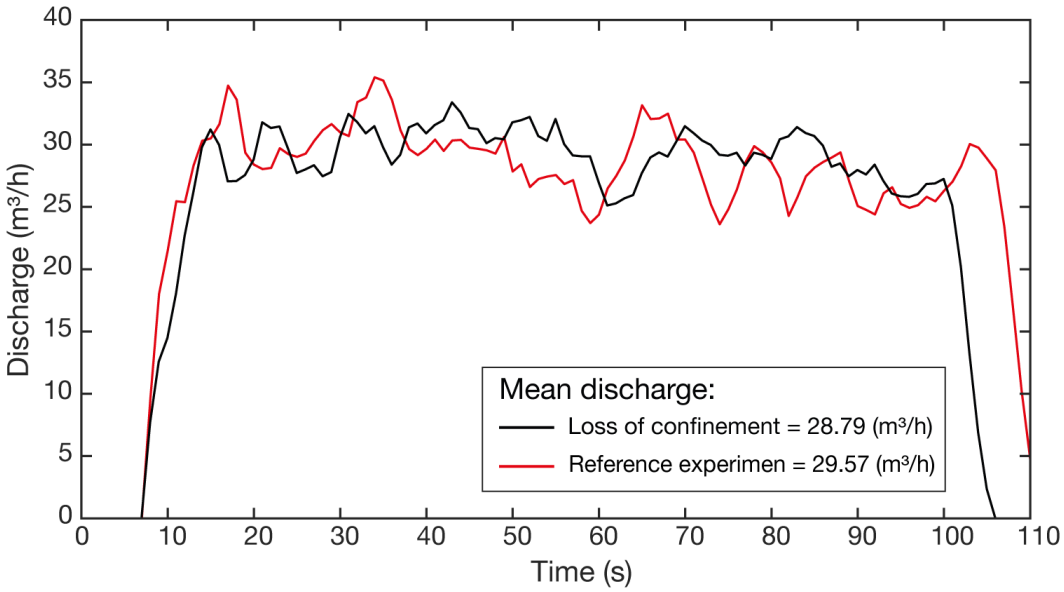

Fig. S4. Discharge measurements of the two experiments. The discharge was measured with an electromagnetic flow-meter (Krohne Optiflux 2300). The mean discharge was calculated by averaging over the time interval between 15 to 95 s.

Manufacturer and type	MET-FLOW; DUO MX
Speed of sound in water (m/s)	1480
Measurement window (mm)	246.79
Number of channels	235
Distance between channel centers (mm)	0.925
Channel width (mm)	3.7
Frequency of the ultrasound beam (MHz)	1
Number of cycles per pulse	5
Number of sound pulses per measurement	32
Minimum on-axis velocity (mm/s)	-1081.9
Maximum on-axis velocity (mm/s)	1073.4
Velocity resolution (mm/s)	8.5
Time between each measurements (s)	1.247

Tab. S1. UVP data acquisition settings.

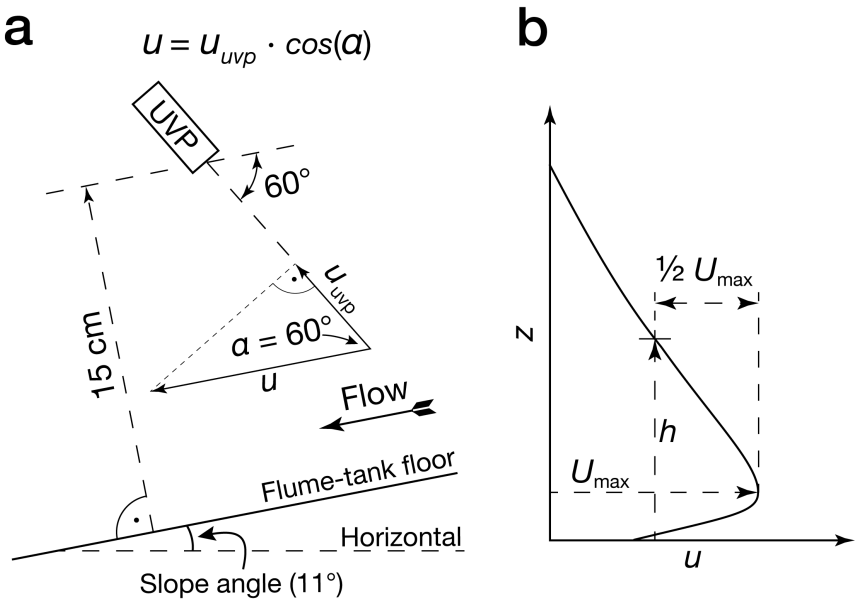

Fig. S5. UVP orientation and parameterization of the velocity profile. a,**b**, (**a**) The orientation of the UVP and the trigonometric calculation to calculate bed-parallel velocities. u_{UVP} is the velocity component directed toward the UVP and u is the bed parallel velocity in downflow direction. Not to scale. (**b**) Sketch of a velocity profile illustrating the analysis of the time-averaged velocity profiles. Redrawn from [50].

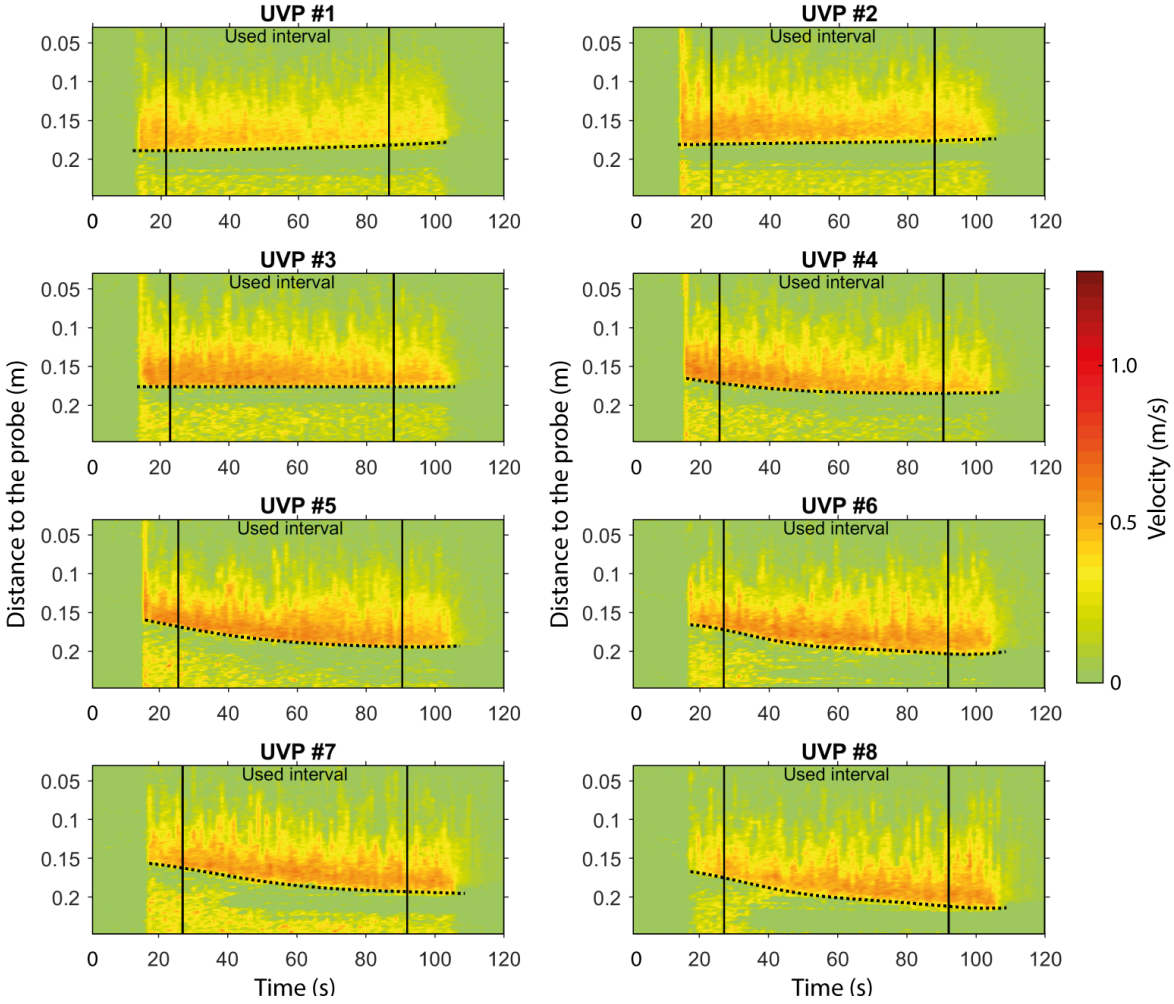

Fig. S6. Velocity measurements in the experiment with loss of confinement. The solid vertical lines mark the interval that was used for analysis of the velocity data. The dashed line indicated the position of the bed, where a sharp decrease in velocity occurs.

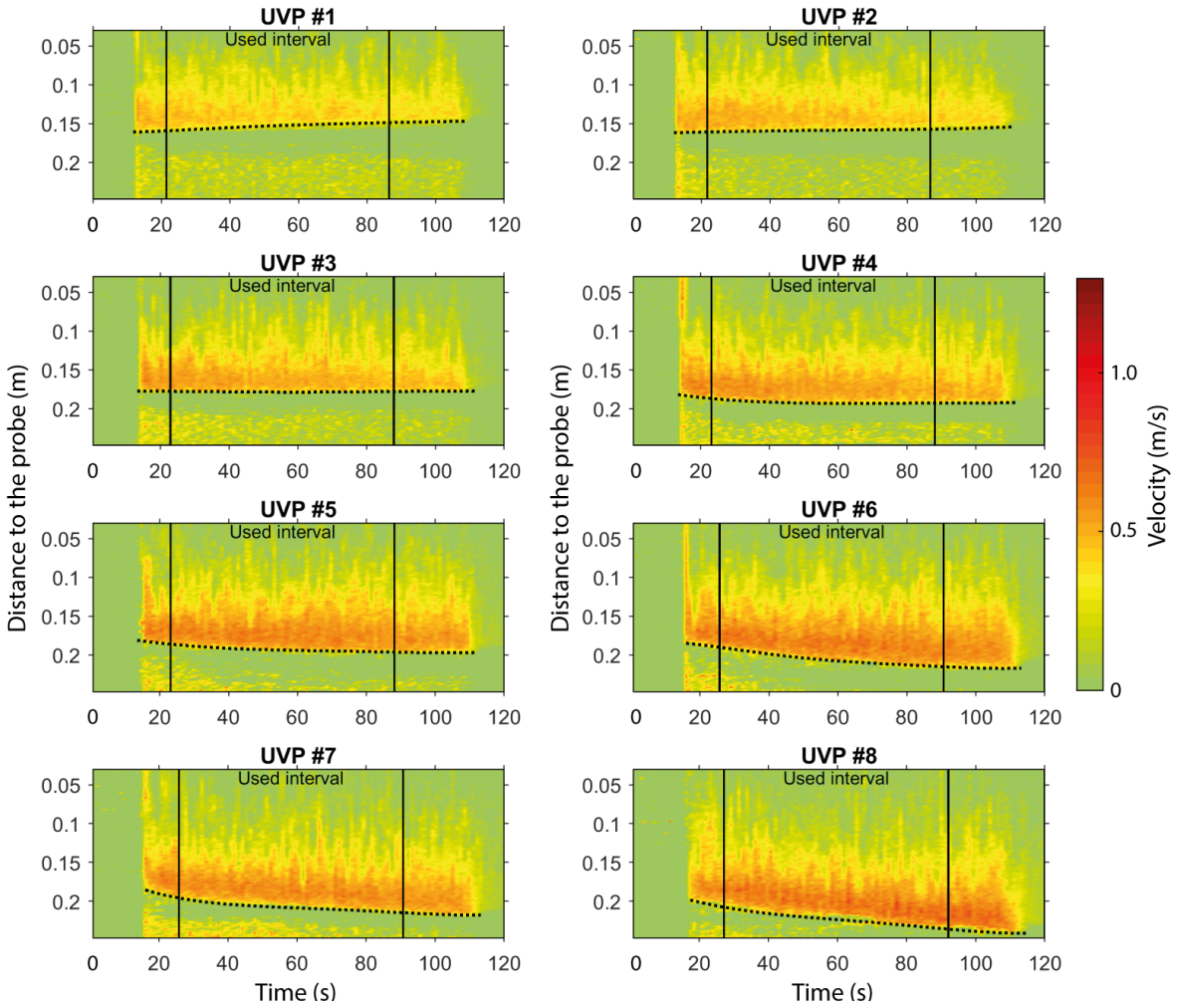

Fig. S7. Velocity measurements in the reference experiment. The solid vertical lines mark the interval that was used for analysis of the velocity data. The dashed line indicated the position of the bed, where a sharp decrease in velocity occurs.

Author contributions

J.T.E. and M.J.B.C. initiated the EuroSEDS project. F.P conducted the experiments, analysed the results and wrote the initial manuscript. All authors contributed to interpretation of the data and writing of the manuscript

Competing interests statement

The authors declare no competing interests.

References

1. Galy, V. *et al.* Efficient organic carbon burial in the Bengal fan sustained by the Himalayan erosional system. *Nature* **450,** 407–410 (2007).
2. Azpiroz-Zabala, M. *et al.* Newly recognized turbidity current structure can explain prolonged flushing of submarine canyons. *Sci. Adv.* **3,** 1–12 (2017).
3. Nilsen, T. H., Shew, R. D., Steffens, G. S. & Studlick, J. R. J. *Studlick, Atlas of Deep-Water Outcrops*. (AAPG Studies in Geology 56 & Shell Exploration & Production. 504 pp., 2008).
4. Pham, C. K. *et al.* Marine litter distribution and density in European seas, from the shelves to deep basins. *PLoS One* **9,** 1–13 (2014).
5. Cressey, D. The Plastic Ocean. *Nature* **536,** 263–265 (2016).
6. Stevenson, C. J., Jackson, C. A.-L., Hodgson, D. M., Hubbard, S. M. & Eggenhuisen, J. T. Deep-Water Sediment Bypass. *J. Sediment. Res.* **85,** 1058–1081 (2015).
7. Bouma, A. H., Normark, W. R. & Barnes, N. E. *Submarine Fans and Related Turbidite Systems*. (Springer. 351 pp., 2012).
8. Mutti, E. & Normark, W. R. Comparing Examples of Modern and Ancient Turbidite Systems: Problems and Concepts. in *Marine Clastic Sedimentology* (eds. Leggett, J. K. & Zuffa, G. G.) 1–38 (Springer, 1987). doi:10.1007/978-94-009-3241-8_1
9. Alexander, J. *et al.* Laboratory sustained turbidity currents form elongate ridges at channel mouths. *Sedimentology* **55,** 845–868 (2008).
10. Stacey, C. D. *et al.* How turbidity current frequency and character varies down a fjord-delta system: Combining direct monitoring, deposits and seismic data. *Sedimentology* **66,** 1–31 (2018).
11. Kenyon, N. H. & Millington, J. Contrasting deep-sea depositional systems in the Bering Sea. in *Atlas of Deep Water Environments* (eds. Pickering, K. T., Hiscott, R. N., Kenyon, N. H., Ricci Lucchi, F. & Smith, R. D. A.) 196–202 (Springer Netherlands, 1995).
12. Macdonald, H. A. *et al.* New insights into the morphology, fill, and remarkable longevity (>0.2 m.y.) of modern deep-water erosional scours along the northeast Atlantic margin. *Geosphere* **7,** 845–867 (2011).
13. Palanques, A., Kenyon, N. H., Alonso, B. & Limonov, A. Erosional and depositional patterns in the Valencia Channel mouth: An example of a modern channel-lobe transition zone. *Mar. Geophys. Res.* **18,** 104–118 (1996).
14. Wynn, R. B., Kenyon, N. H., Masson, D. G., Stow, D. A. V. & Weaver, P. P. E. Characterization and recognition of deep-water channel-lobe transition zones. *Am. Assoc. Pet. Geol. Bull.* **86,** 1441–1462 (2002).
15. Dorrell, R. M. *et al.* Flow dynamics and mixing processes in hydraulic jump arrays: Implications for channel-lobe transition zones. *Mar. Geol.* **381,** 181–193 (2016).
16. Yu, B. *et al.* Experiments on Self-Channelized Subaqueous Fans Emplaced by Turbidity Currents and Dilute Mudflows. *J. Sediment. Res.* **76,** 889–902 (2006).
17. Hodgson, D. M., Kane, I. A., Flint, S. S., Brunt, R. L. & Ortiz-Karpf, A. Time-Transgressive Confinement On the Slope and the Progradation of Basin-Floor Fans: Implications For the Sequence Stratigraphy of Deep-Water Deposits. *J. Sediment. Res.* **86,** 73–86 (2016).

18. Metivier, F., Lajeunesse, E. & Cacas, M.-C. Submarine Canyons in the Bathtub. *J. Sediment. Res.* **75,** 6–11 (2005).

19. Fildani, A. *et al.* Erosion at inception of deep-sea channels. *Mar. Pet. Geol.* **41,** 48–61 (2013).

20. Hamilton, P. B., Strom, K. B. & Hoyal, D. C. J. D. Hydraulic and sediment transport properties of autogenic avulsion cycles on submarine fans with supercritical distributaries. *J. Geophys. Res. F Earth Surf.* **120,** 1369–1389 (2015).

21. Komar, P. D. Hydraulic jumps in turbidity currents. *Bull. Geol. Soc. Am.* **82,** 1477–1488 (1971).

22. Macdonald, R. G. *et al.* Flow patterns, sedimentation and deposit architecture under a hydraulic jump on a non-eroding bed: Defining hydraulic-jump unit bars. *Sedimentology* **56,** 1346–1367 (2009).

23. Chanson, H. *Hydraulics of open channel flow*. (Elsevier. 650 pp., 2004).

24. Russell, H. a J. & Arnott, R. W. C. Hydraulic-Jump and Hyperconcentrated-Flow Deposits of a Glacigenic Subaqueous Fan: Oak Ridges Moraine, Southern Ontario, Canada. *J. Sediment. Res.* **73,** 887–905 (2003).

25. de Leeuw, J., Eggenhuisen, J. T. & Cartigny, M. J. B. Morphodynamics of submarine channel inception revealed by new experimental approach. *Nat. Commun.* **7,** 1–7 (2016).

26. Eggenhuisen, J. T. & McCaffrey, W. D. Dynamic deviation of fluid pressure from hydrostatic pressure in turbidity currents. *Geology* **40,** 295–298 (2012).

27. de Leeuw, J., Eggenhuisen, J. T. & Cartigny, M. J. B. Linking submarine channel–levee facies and architecture to flow structure of turbidity currents: insights from flume tank experiments. *Sedimentology* **65,** 931–951 (2018).

28. Hofstra, M., Hodgson, D. M., Peakall, J. & Flint, S. S. Giant scour-fills in ancient channel-lobe transition zones: Formative processes and depositional architecture. *Sediment. Geol.* **329,** 98–114 (2015).

29. Garcia, M. & Parker, G. Experiments on hydraulic jumps in turbidity currents near a canyon-fan transition. *Science (80-.).* **245,** 393–396 (1989).

30. Sumner, E. J. *et al.* First direct measurements of hydraulic jumps in an active submarine density current. *Geophys. Res. Lett.* **40,** 5904–5908 (2013).

31. Paull, C. K. *et al.* Powerful turbidity currents driven by dense basal layers. *Nat. Commun.* **9,** 4114 (2018).

32. Tilston, M., Arnott, R. W. C., Rennie, C. D. & Long, B. The influence of grain size on the velocity and sediment concentration profiles and depositional record of turbidity currents. *Geology* **43,** 839–842 (2015).

33. Sequeiros, O. E. *et al.* Characteristics of Velocity and Excess Density Profiles of Saline Underflows and Turbidity Currents Flowing over a Mobile Bed. *J. Hydraul. Eng.* **136,** 412–433 (2010).

34. Allen, J. R. L. Transverse erosional marks of mud and rock: their physical basis and geological significance. *Sediment. Geol.* **5,** 167–385 (1971).

35. Klaucke, I., Hesse, R. & Ryan, W. B. F. F. Morphology and structure of a distal submarine trunk channel: The Northwest Atlantic Mid-Ocean Channel between lat 53°N and 44°30′N. *Bull. Geol. Soc. Am.* **110,** 22–34 (1998).

36. Jegou, I., Savoye, B., Pirmez, C. & Droz, L. Channel-mouth lobe complex of the recent Amazon Fan: The missing piece. *Mar. Geol.* **252,** 62–77 (2008).

37. Hughes Clarke, J. E. *et al.* The Squamish ProDelta : Monitoring Active Landslides and Turbidity Currents. *Can. Hydrogr. Conf. 2012* 1–15 (2012).

38. Straub, K. M. & Mohrig, D. Quantifying the morphology and growth of levees in aggrading submarine channels. *J. Geophys. Res. Earth Surf.* **113,** 1–20 (2008).

39. Brucker, S. *et al.* Monitoring flood-related change in bathymetry and sediment distribution over the Squamish Delta, Howe Sound, British Columbia. *U.S. Hydrogr. Conf.* 1–16 (2007).

40. Zhong, G., Cartigny, M. J. B., Kuang, Z. & Wang, L. Cyclic steps along the South Taiwan Shoal and West Penghu submarine canyons on the northeastern continental slope of the South China Sea. *Bull. Geol. Soc. Am.* **127,** 804–824 (2015).

41. Shields, A. Anwendung der Aehnlichkeitsmechanig und der Turbulenzforschung auf die Geschiebebewegung. *Mitteilungen der Preußischen Versuchsanstalt für Wasserbau und Schiffbau* **26,** (Technische Hochschule Berlin, 25 pp, 1936).

42. Middleton, G. V & Southard, J. B. *Mechanics of Sediment Movement*. **3,** (SEPM, Eastern Section Short Course 3 Providence, 401 pp., 1984).

43. van Rijn, L. C. *Principles of sediment transport in rivers, estuaries and coastal seas*. *Aqua publications* (Aqua publications. 790 pp., 1993). doi:10.1002/9781444308785

44. Cartigny, M. J. B., Eggenhuisen, J. T., Hansen, E. W. M. & Postma, G. Concentration-Dependent Flow Stratification In Experimental High-Density Turbidity Currents and Their Relevance To Turbidite Facies Models. *J. Sediment. Res.* **83,** 1046–1064 (2013).

45. Xu, J. P. Normalized velocity profiles of field-measured turbidity currents. *Geology* **38,** 563–566 (2010).

46. Garcia, M. Sedimentation Engineering: Processes, Measurements, Modeling and Practise. *Am. Soc. Civ. Eng.* 1132 pp. (2008).

47. Xu, J. P., Sequeiros, O. E. & Noble, M. A. Sediment concentrations, flow conditions, and downstream evolution of two turbidity currents, Monterey Canyon, USA. *Deep. Res. Part I Oceanogr. Res. Pap.* **89,** 11–34 (2014).

48. Buckee, C., Kneller, C. & Peakall, J. Turbulence structure in steady, solute-driven gravity currents. in *Particulate gravity currents* (eds. Mccaffrey, W. D., Kneller, B. & Peakall, J.) 173–188 (International Association of Sedimentologists, Special Publication 31, Blackwell Science, 2001).

49. Kneller, B. & Buckee, C. The structure and fluid mechanics of turbidity currents: a review of some recent studies and their geological implications. *Sedimentology* **47,** 62–94 (2000).

50. Launder, B. E. & Rodi, W. The Turbulent Wall Jet Measurements and Modeling. *Annu. Rev. Fluid Mech.* **15,** 429–459 (1983).

51. Gray, T. E., Alexander, J. & Leeder, M. R. Quantifying velocity and turbulence structure in depositing sustained turbidity currents across breaks in slope. *Sedimentology* **52,** 467–488 (2005).

52. Bagnold, R. A. *An Approach to the Sediment Transport Problem from General Physics. USGS Professional Paper 422-1* (USGS Professional Paper 422-1, U.S. Government Printing Office, 1966). doi:10.1017/S0016756800049074

53. Nino, Y., Lopez, F. & Garcia, M. Threshold for particle entrainment into suspension. *Sedimentology* **50,** 247–263 (2003).